Thesis for the degree of Licentiate of Engineering

Aerodynamic Design and Experimental Investigation of Short Nacelles for Future Turbofan Engines

Vinícius Tavares Silva

Department of Mechanics and Maritime Sciences
CHALMERS UNIVERSITY OF TECHNOLOGY
Göteborg, Sweden 2020

Aerodynamic Design and Experimental Investigation of Short Nacelles for Future Turbofan Engines
Vinícius Tavares Silva

Licentiatavhandlingar vid Chalmers tekniska högskola
Technical report No. 2020:20
ISSN 1652-8565

Department of Mechanics and Maritime Sciences
Chalmers University of Technology
SE–412 96 Göteborg, Sweden
Telephone + 46 (0) 31 – 772 1000

Cover: Ultra-short nacelle configuration showing the contours of static temperature on the captured and post-exit streamtubes

Typeset by the author using LaTeX.

Printed by Chalmers Reproservice
Göteborg, Sweden 2020

"The essence of an individual's freedom is the opportunity to deviate from traditional ways of thinking and of doing things."
(Ludwig von Mises).

Abstract

Aerodynamic Design and Experimental Investigation of Short Nacelles for Future Turbofan Engines
Thesis for the degree of Licentiate of Engineering in Thermo and Fluid Dynamics
VINÍCIUS TAVARES SILVA
Department of Mechanics and Maritime Sciences
Division of Fluid Dynamics
Chalmers University of Technology

To achieve a higher propulsive efficiency, and hence reduced fuel burn and emissions, the next generation turbofan engines are expected to have higher bypass ratios and lower fan pressure ratios. However, the larger the bypass ratio, the larger becomes the fan and thus the nacelle. The result is an undesired increase in weight and nacelle drag. For this reason, advanced nacelle designs with shorter inlets and exhaust nozzles are necessary, so that the attained performance benefits are not outweighed by the increased installation drag and weight.

This thesis presents a newly developed methodology for multi-point design of ultra-short nacelles. An integrated aerodynamic framework, based on parametric geometry generation and computational fluid dynamics (CFD) flow solutions was built and used for designing several ultra-short nacelle shapes and to evaluate their aerodynamic performance. The main design parameters and their influence in the flow field were investigated for the most critical operating conditions among the flight mission, such as cruise, high angle-of-attack (AoA) and crosswind. The aerodynamic performance of the designed nacelles was evaluated through a thrust and drag bookkeeping approach, and also by means of the distortion levels at the fan face.

Furthermore, this work summarizes the main results obtained in an experimental aerodynamic investigation of a powered turbofan nacelle, conducted at the Chalmers low-speed wind tunnel. The impact of the engine angle-of-attack and the mass flow ratio (MFR) on the nacellle aerodynamic performance was investigated.

Keywords: Ultra-short nacelles, ultra-high-bypass turbofan, thrust-and-drag bookkeeping, Computational Fluid Dynamics, experimental, powered nacelle.

Acknowledgments

I would like to thank Anders Lundbladh for the excellent supervision, for the bright ideas that he has always been wiling to share and for the long and insightful discussions. Thanks to Tomas Grönstedt for the opportunity of pursuing my PhD. To Olivier Petit for all the support in my first year and to Carlos Xisto for the recent, but already very helpful supervision. To Isak Jonsson and Valery Chernoray for all the help in the lab.

I would also like to acknowledge my family for supporting my choice of moving to somewhere so far away from home and, last but not least, thanks to all my colleagues in the Fluid Dynamics Division at Chalmers, for creating such a friendly and pleasant work environment.

This research work was funded by the Swedish National Aviation Engineering Research Program, NFFP, supported by Swedish Armed Forces, the Swedish Defense Materiel Administration, Swedish Governmental Agency for Innovation Systems (VINNOVA) and GKN aerospace. All the computations were performed using C3SE (Chalmers Center for Computational Science and Engineering) resources, provided by SNIC (Swedish National Infrastructure for Computing).

Vinícius Tavares Silva
Göteborg, December 2020

List of Publications

This thesis is based on the following appended paper:

Paper 1. Vinícius Tavares Silva, Anders Lundbladh, Carlos Xisto, Olivier Petit *Multi-point Aerodynamic Design of Ultra-short Nacelles for Ultra-high Bypass Turbofan Engines.* To be submitted (2020).

Nomenclature

Latin

A_{fan}	–	Fan face area
BP_n	–	Bernstein polynomial of order n
$C(\psi)$	–	Class function
C_D	–	Discharge coefficient
C_p	–	Pressure coefficient
$C_{l_{max}}$	–	Maximum lift coefficient
DC_{60}	–	Total pressure distortion parameter
D_c	–	Configuration drag
D_{FC}	–	Fan cowl drag
D_{fan}	–	Fan diameter
D_{scrub}	–	Scrubbing drag
F_N	–	Net propulsive force
F_{pre}	–	Pre-entry force
$K_{i,n}$	–	Binomial coefficients
L	–	Length
Ma	–	Mach number
Ma_{is}	–	Isentropic Mach number
Ma_{max}	–	Maximum Mach number
$\overline{P}_{0,60}$	–	Average total pressure at 60deg sector
$\overline{P}_{0,fan}$	–	Average total pressure at the fan face
R	–	Radius of curvature
S	–	Bookkeeping boundary surfaces
$S(\psi)$	–	Shape function
T_N	–	Standard net thrust
a	–	Lip length
b	–	Lip height
bp_i	–	Bernstein weighting coefficients
c	–	Chord
c_d	–	Drag coefficient
f_{le}	–	Non-dimensional leading edge radius of curvature
f_{cpr}	–	Lip control point radial position
f_{cpx}	–	Lip control point axial position
$\vec{i}$	–	Axial unity vector

$\vec{n} = [n_x, n_y, n_z]$	–	Normal vector
p	–	Static pressure
$\overline{q}$	–	Average dynamic pressure
$\vec{V} = [u, v, w]$	–	Velocity vector
x, r, ϕ	–	Cylindrical coordinates

Greek

β_{te}	–	Nacelle boattail angle
ρ	–	Density
$\vec{\tau}_x = [\tau_{xx}, \tau_{xy}, \tau_{xz}]$	–	Axial viscous stress vector
θ_d	–	Droop angle

Subscripts

0	–	Captured stream-tube entry station
1	–	Inlet entry station
13	–	Fan outlet station
18	–	Bypass nozzle exhaust station
2	–	Fan face station
8	–	Core nozzle exhaust station
BN	–	Bypass nozzle
CC	–	Core cowl
CN	–	Core nozzle
FC	–	Fan cowl
I	–	Inlet
P	–	Plug
S	–	Spinner
hi	–	Highlight
max	–	Position of maximum radius
nozz	–	Nozzle
te	–	Trailing edge
th	–	Throat
∞	–	Freestream

Abbreviations

ACARE	–	Advisory Concil for Aviation Research and Innovation
AoA	–	Angle of attack
BC	–	Boundary conditions
BPR	–	Bypass ratio
CFD	–	Computational fluid dynamics

CST	–	Class shape transformation
EDF	–	Electric ducted fan
FPR	–	Fan pressure ratio
MFR	–	Mass flow ratio
RANS	–	Reynolds-averaged Navier-Stokes
SST	–	Shear-stress transport
UHBP	–	Ultra-high bypass
WS	–	Wind speed

Contents

Part I

Introductory chapters

Chapter 1

Introduction

In civil aviation there has been a constant push for reducing fuel burn, noise and environmental impact. The Advisory Council for Aviation Research and Innovation in Europe (ACARE) has established ambitious goals in Flightpath 2050, including reductions of 75% in CO_2 emissions, 65% in perceived noise and 90% in NOx emissions, relative to a typical year-2000 aircraft [1]. To achieve such challenging objectives, the current aero-engines will need to undergo severe technology modifications. In order to achieve a higher overall efficiency, it is necessary to enhance the engine's thermal and propulsive efficiencies simultaneously. The former can be raised by improving the performance of the core components, by increasing the burner exit temperature and the overall pressure ratio. The latter can be achieved by employing higher bypass ratios (BPR) and lower fan pressure ratios (FPR). Figure 1.1 shows the evolution of aero-engines efficiencies. It is easily notable that the propulsive efficiency progresses followed by an increase in BPR.

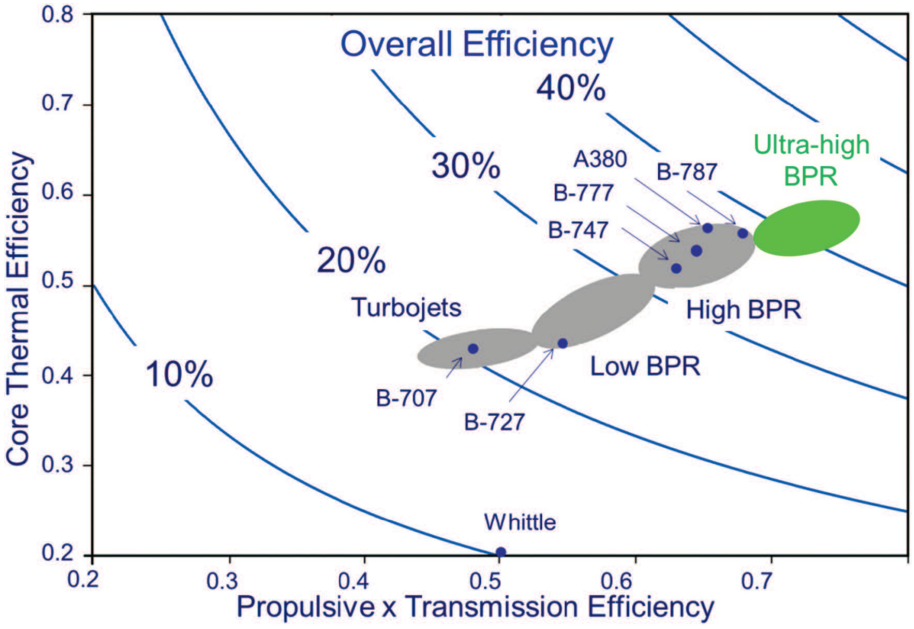

Figure 1.1: Evolution of aero-engines efficiency [2].

The next generation turbofan engines are expected to operate with BPR greater than 15, referred to as Ultra High Bypass Ratio (UHBP), and FPRs lower than 1.4. This can be achieved through the geared-turbofan architecture, which features a gearbox between the fan and the low pressure compressor. In addition, substantial noise reduction can be obtained with the low FPR and low fan speeds. It can be seen in Fig. 1.2 that the geared turbofan allows a shift in the minimum fuel burn and a substantial reduction in noise.

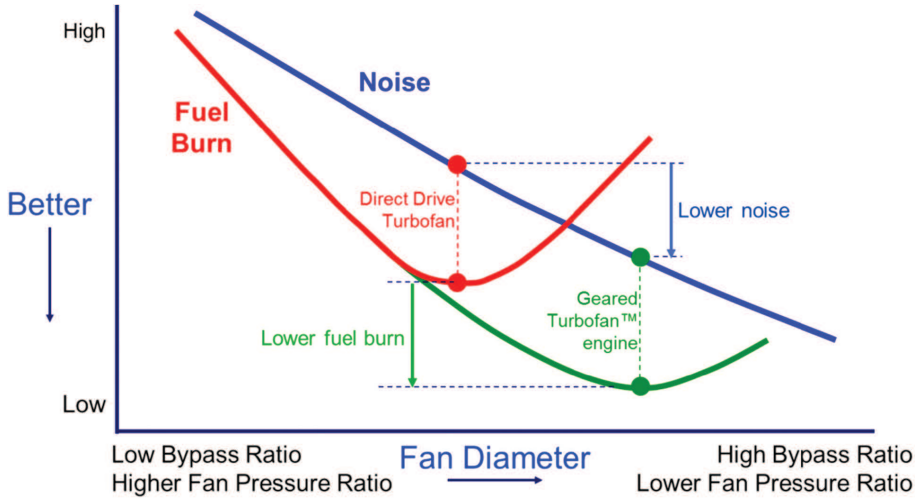

Figure 1.2: Fuel burn and noise characteristics of advanced turbofan engines [2].

Nonetheless, such configurations require large fan diameters, which result in increased nacelle wetted area, and hence, drag. Therefore, advanced nacelle designs, with shorter inlets and exhaust nozzles, are required so that the gain in propulsive efficiency is not outweighed by the higher installation drag and weight.

State-of-the-art turbofan engines feature intakes with inlet length over fan diameter ratios (L_I/D_{fan}) laying between 0.5 and 0.65. However, future aero-engines will probably have inlets with (L_I/D_{fan}) substantially below 0.5. As the inlets shorten, their design becomes substantially more challenging, mainly for low-speed and high incidence conditions. Since short inlets have reduced internal diffusion capability, boundary layer separation is likely to occur, leading to poor performance and engine instability.

1.1 Aim of the Study

The focus of this work is to provide a step further on the design of ultra-short nacelles for UHBP turbofan engines. This will by achieved through the completion of the following objectives:

- Establishing a novel methodology for multi-point design of ultra-short nacelles for UHBP turbofan engines;
- studying the flow field around nacelles under operating conditions considered to be critical for the engine's performance and stability;

- identifying the major design parameters in each of the operating conditions and how they impact the flow field end engine's performance;
- designing geometries which provide good performance trade-offs between the high and low-speed flow conditions, and highlighting important decisions to be taken during the design procedure.

A secondary goal of this thesis is to present the initial results of an experimental aerodynamic investigation on a powered nacelle rig, conducted at the Chalmers low-speed wind tunnel.

Chapter 2

General Aspects of Nacelle Design

2.1 Previous work

The design of high-bypass ratio turbofan nacelles has been subject of research since the early 60's. The methods for shaping nacelles can be split into two categories: parametric and inverse design. The former consists of building the nacelle based on pre-defined aerodynamic shapes, such as airfoil profiles or splines [3–12]. The latter consists of adapting the nacelle form for attaining a targeted pressure distribution [13–16]. As the civil aero-engines get larger, the more crucial it becomes to severely reduce drag. This can be done either by shortening the inlets and exhaust nozzles [17–19], by achieving natural or hybrid laminar flow over the nacelles [20–24], or a combination of both.

Considerable achievements in modern nacelle design were reached over the last decade. Cristie et al. [25, 26] and Lundbladh et al. [27] have developed new Class Shape Transformation (CST) based approaches for designing nacelle and intake aerolines, and Tajero et al. [28–30] have developed CST based methods for 3D nacelles shape multi-objective optimization. Furthermore, CST curves were also widely used for exhaust nozzles design and optimization [31–33]. However, so far, the presented CST methodologies were employed either to design 2D asymmetric nacelle shapes, or to design 3D shapes considering only flight conditions under the cruise segment, and thus neglecting other critical conditions within the flight envelope. Therefore, the CST method capability was not yet explored for designing 3D asymmetric geometries capable of performing well under the most critical flight conditions. Besides, the CST method was not yet applied to the design of ultra-short nacelles, with L_I/D_{fan} below 0.4.

Peters et al. [17] have presented a spline-based framework for designing nacelles with ultra-short inlets and assessed the performance of different short inlet candidates compared to a standard length baseline. Rainer Schnell et al. [18] presented coupled fan-intake design methodology for potential application to ultra-short intakes for UHBP engines.

Extensive research has been conducted on nacelles subjected to crosswinds [34–37]. Although some studies considering crosswind effects on short inlets exist [17–19], not much has been explored on how crosswind can impact the design of ultra-short

nacelles. Furthermore, the design of nacelles with ultra-short inlets remains an under-exploited area, since not much can be found in the literature besides the work presented in [17, 18].

This thesis is built on the aforementioned research, providing a novel CST based methodology for multi-point design of ultra-short nacelles. The design procedure consider 3D effects of both asymmetric geometries and asymmetric flow field under the most critical conditions that are expected to occur for a given aircraft mission, such as cruise, high angle-of-attack and crosswind. Moreover, a step further is achieved on this under-exploited area, which is the design of ultra-short nacelles, by a thorough assessment of the impact of the major design parameters on the flow field for the selected operating conditions.

2.2 Aerodynamic design considerations

The design of a turbofan nacelle requires several compromises, since the optimum shape will be different for different operating conditions within the flight envelope [38, 39]. Figure 2.1 shows a schematic representation of the flow field under different operating conditions and some possible flow phenomena that might occur.

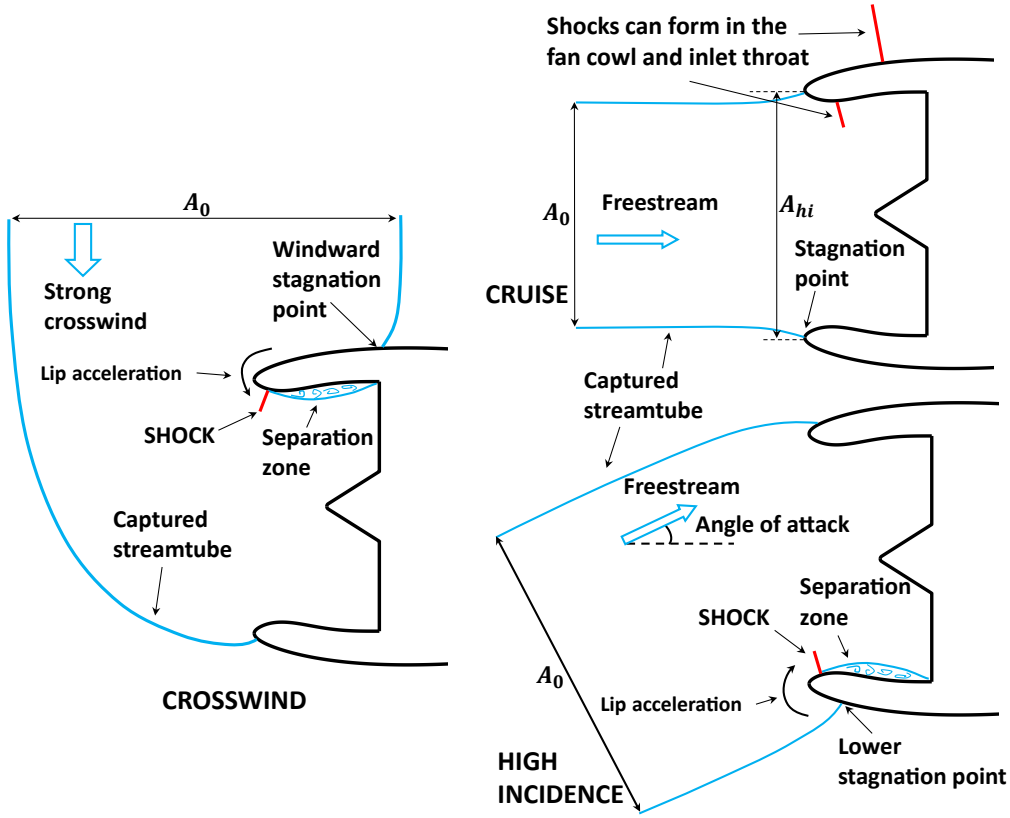

Figure 2.1: Schematic representation of the flow field for different operating conditions: cruise, crosswind and high incidence.

For cruise the focus should be minimizing drag, therefore, the supersonic velocities at the fan cowling should be limited and shock waves should be avoided when possible,

since they are accompanied by significant increase in wave drag. Internally in the inlet, shock waves can also be formed, causing excessive boundary layer thickening and increased loss in intake pressure recovery η_i. In the most severe cases, shock-induced separation can occur and thus the throat area should be selected to avoid the occurrence of such shocks [38–40].

A reference aerodynamic parameter for the inlet is the mass flow ratio MFR, which is defined as the the ratio between the streamtube captured area A_0 and the highlight area A_{hi}. Typical values of MFR will vary between 0.7 and 0.8 for cruise. At low-speeds, the MFR will be larger than one and the highest velocities will occur internally in the inlet. Particularly at high incidence, the lower stagnation point will be somewhere outside the lip and thus the flow need to accelerate around the lip, which results in strong shocks downstream of the highlight position. This frequently results in shock induced separation. For crosswind the MFR is the greatest and the windward stagnation point is now located somewhere in the fan cowling. This requires the flow to be severely deflected in order to enter the inlet duct. Two types of separation can occur for this case: the first happens for low-speeds and is primarily driven by excessive diffusion, starting near the highlight position; the second takes place for high fan speeds and high inlet mass flows, when a shock wave is formed internally in the windward lip and the strong adverse pressure gradient causes the flow to separate.

The conflicting requirements existing for different flight conditions result in a asymmetric nacelle shape. The inlet is thus thinner on its top part to avoid excessive wave drag, whilst its lower part is thicker and rounder, to prevent high-incidence separation and to alleviate distortion.

Excessive drag can result from the bypass jet and the external streams interaction. If the nozzle is choked, the exhaust pressure will be higher than the ambient pressure and strong adverse pressure gradients can develop in the fan cowl, which can generate a small separation region and increase drag substantially. The drag developed by the rear part of the fan cowl is termed boat tail drag and a proper boat tail angle β_{te} should be selected to minimize it.

Chapter 3

Methods

3.1 Geometry Generation

3.1.1 Class Shape Transformation Method

Class Shape Transformation (CST) curves were used to generate the nacelle geometries presented in this work. The CST method [41, 42] consists of a robust and versatile approach for parametric representation of aerodynamic shapes, which allows the construction of smooth and complex geometries with not many design variables. The CST method has recently been applied to the design of nacelles for modern turbofan engines [25, 43–45]. It can be mathematically represented by the product of a class function $C(\psi)$ and a shape function $S(\psi)$, as follows:

$$\xi\left(\psi\right) = S\left(\psi\right) C\left(\psi\right) + \psi \Delta\xi_{te}\,, \tag{3.1}$$

where $\xi = r/c$, $\psi = x/c$ and the term $\psi\Delta\xi_{te}$ modifies the trailing edge's radial coordinate.

The class function, which determines the basic profile, is defined as

$$C\left(\psi\right) = \psi^{N1}\left(1-\psi\right)^{N2}\,. \tag{3.2}$$

The exponents N_1 and N_2 in Eq. (3.2) are used to define the class of the geometric shape. For a round nose and a sharp trailing edge, $N_1 = 0.5$ and $N_2 = 1$.
The shape function is used to transform the class function and can be represented by a nth order Bernstein polynomial, defined as

$$BP_n\left(\psi\right) = \sum_{i=0}^{n}\left[K_{i,n}\cdot\left(\psi^i\left(1-\psi\right)^{n-i}\right)\right]\,, \tag{3.3}$$

where $K_{i,n}$ are the binomial coefficients

$$K_{i,n} = \frac{n!}{i!(n-i)!}\,. \tag{3.4}$$

The shape function final form is then attained by multiplying Eq.(3.3) by weighting coefficients, bp_i

$$S(\psi) = \sum_{i=0}^{n} \left[bp_i \cdot K_{i,n} \cdot \left(\psi^r (1-\psi)^{n-i} \right) \right] . \tag{3.5}$$

The first weighting coefficient, bp_0, is directly related to the highlight radius of curvature, R_{le}, by the relation

$$bp_0 = \sqrt{\frac{2R_{le}}{c}} . \tag{3.6}$$

The last weighting coefficient bp_n is related to the bottail angle added to a term to modify the trailing edge's radial coordinate, as follows

$$bp_n = \tan(\beta_{te}) + \frac{\Delta\xi_{te}}{c} . \tag{3.7}$$

To calculate the remaining weighting coefficients and hence to fully define $\xi(\psi)$, a set of constraints must be defined, which can be either control points or derivatives. Once these constraints are specified, a $(n-1)$ by $(n-1)$ linear set of equations is formed from Eq. (3.1) and its derivatives $\xi(\psi)'$ and $\xi(\psi)''$. After solving the system, the CST curves are determined.

3.1.2 Parametric Geometry Representation

A 2D nacelle geometry can be fully defined by joining six different CST curves, representing the inlet, fan cowl, bypass and core nozzle outer parts, core cowl, core nozzle and plug. This section provides a brief description on how the CST curves are parametrized.

The main parameters for the inlet and fan cowl geometric representation are depicted in Figure 3.1.

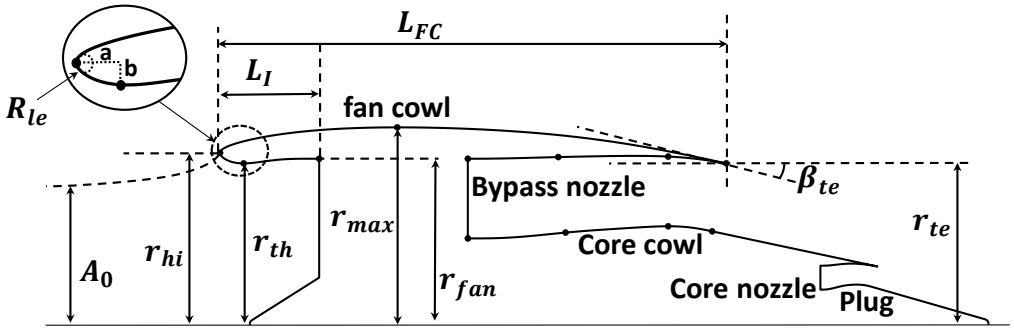

Figure 3.1: Fan cowl and inlet main geometric parameters.

The fan cowl is defined by a 4th order Bernstein polynomial. As mentioned previously, R_{le}, β_{te} are set as inputs to directly calculate the first and last weighting coefficients. Moreover, constraints are set on the first derivative of the point of maximum radius r_{max} and on the second derivative at the trailing edge, both being equal to zero. Similar constraints are defined for the inlet, with the only difference that the point with first derivative equal to zero is set on the throat position. The

class function coefficients N_1 and N_2 were respectively set as 0.5 and 1.0 for both the fan cowl and inlet. Figure 3.2 shows the constraints employed to the inlet and fan cowl. The control points are highlighted in red.

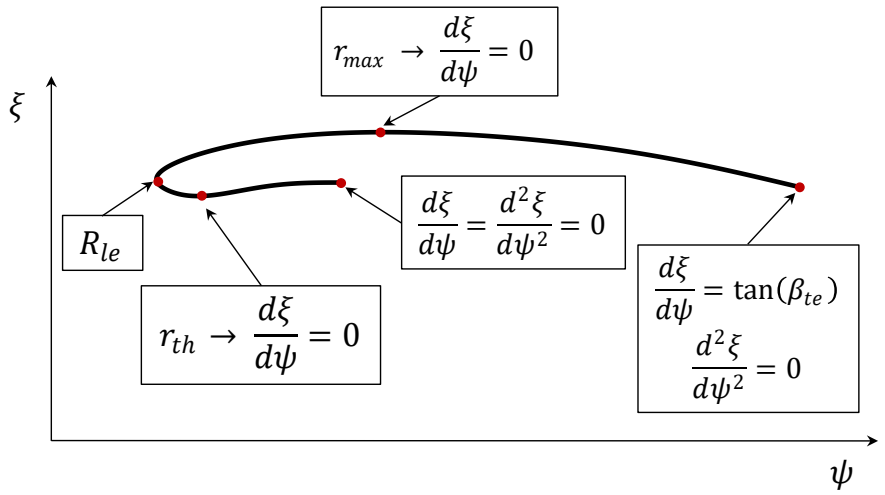

Figure 3.2: Constraints definition for the inlet and fan cowl.

The main input design parameters for the fan cowl and inlet are described in Table 3.1.

Both the bypass and core nozzles are constructed by gathering 2 different CST curves, which define the nozzles' inner and outer parts. The main geometric parameters for representing the bypass nozzle are depicted in Figure 3.3. The parametrization of the core nozzle is analogue to the bypass nozzle and thus will not be described here. The shape function which defines the outer part of the bypass nozzle was set to be a 6th order Bernstein polynomial, whilst for the inner part (core cowl) a 7th order function was selected.

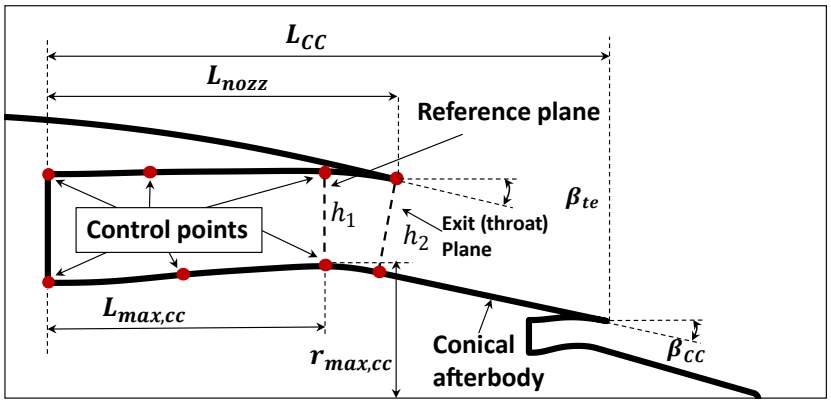

Figure 3.3: Bypass nozzle main geometric parameters.

As it can be seen in Fig. 3.4, the first and second derivatives are constrained to zero at the initial axial position. Furthermore, a second derivative equal to zero is set at the end of the CST curves, together with the boattail angle β. For the core

Table 3.1: Fan cowl and inlet design parameters

Parameter	Description
L_I/D_{fan}	Inlet length to fan diameter ratio
r_{hi}^2/r_{th}^2	Contraction ratio
a/b	Lip aspect ratio
r_{hi}/r_{max}	Highlight radius to maximum radius ratio
r_{max}/r_{fan}	Maximum radius to fan radius ratio
$f_{max} = x_{max}/L_{FC}$	Axial position of maximum diameter
$f_{le} = \frac{R_{le} f_{max} L_{FC}}{(r_{max} - r_{hi})^2}$	Non-dimensional leading-edge radius of curvature
β_{te}	Nacelle boattail angle
θ_{droop}	Inlet droop

cowl, the first derivative is defined to be zero a the point of maximum radius $r_{max,cc}$. The class function coefficients were chosen as $N_1 = 0$ and $N_2 = 1$ for both the inner and outer parts of the nozzles. The main input design parameters for the bypass nozzle are described in Table 3.2.

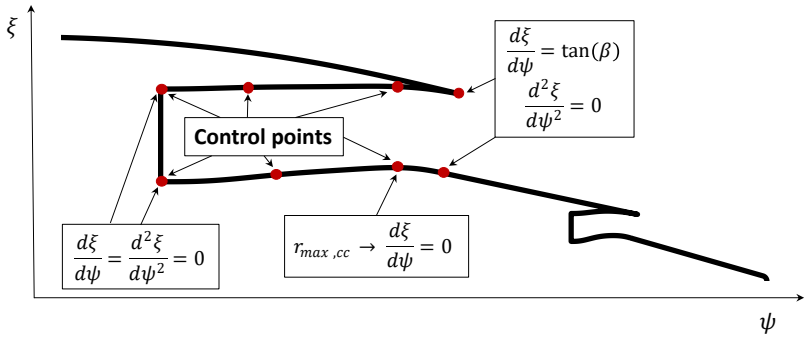

Figure 3.4: Constraints definition for the bypass nozzle.

3.1.3 3D Geometry Generation

A full 3D nacelle geometric representation is shown in Fig. 3.5. Two dimensional parametrizations are performed for the locations of $\phi = 0^o$, $\phi = 90^o$ and $\phi =$

Table 3.2: Bypass nozzle main design parameters

Parameter	**Description**
L_{nozz}/D_{fan}	Bypass duct length to fan diameter ratio
h_1/h_2	Nozzle area ratio
$r_{max,cc}/r_{fan}$	Maximum core cowl radius to fan diameter ratio
β_{cc}	Core cowl trailing edge angle
L_{cc}/D_{fan}	Core cowl length to fan diameter ratio
$f_{max,cc}$	Axial position of maximum radius in the core cowl
$f_{max,cpx}$	Relative axial position of a given control point
$f_{max,cpr}$	Relative radial position of a given control point

180^o, referred to as crown, maximum half-breadth (MHB) and keel, where ϕ is the azimuth angle in a cylindrical coordinate system. In order to obtain a 3D nacelle shape, sinusoidal interpolations in r (radial coordinate) and x (axial coordinate) are performed circumferentially between the crown, MHB and keel. The second nacelle half ($180^o \leq \phi \leq 0^o$) is geometrically symmetric to the first one.

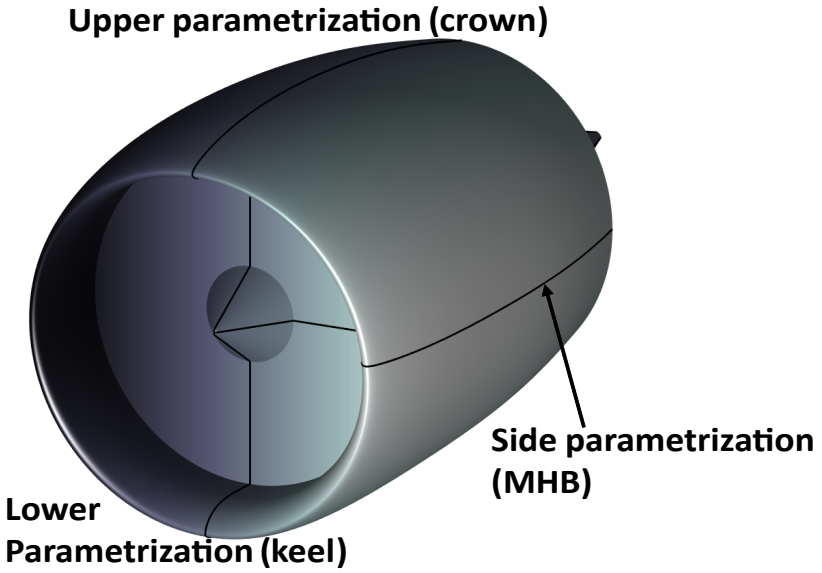

Figure 3.5: Nacelle 3D geometry definition.

The aforementioned locations were strategically selected to allow geometric control where the local flow effects are expected to be critical. At the crown, the highest supersonic speeds are encountered and thus the strongest shocks are formed. Furthermore, the keel and MHB geometries play a fundamental role in preventing flow separation at high angle of attack and crosswind conditions.

An important feature existent in modern turbofan engines is a droop to align the inlet with the wing upwash at cruise [46–48]. A modification was applied to the CST parametrization in order to droop the nacelle inlet over a specified angle θ_{droop}. The crown and keel highlight positions are rotated around a pivoting point located at the intersection between the fan face plane and the engine centerline. A shape deformation function is then applied to the original CST curves so that the fan cowl and inlet shapes are stretched to the new drooped highlight position, proportional to a quadratic function of the axial distance from the pivoting point. The drooping procedure is illustrated in in Fig. 3.6.

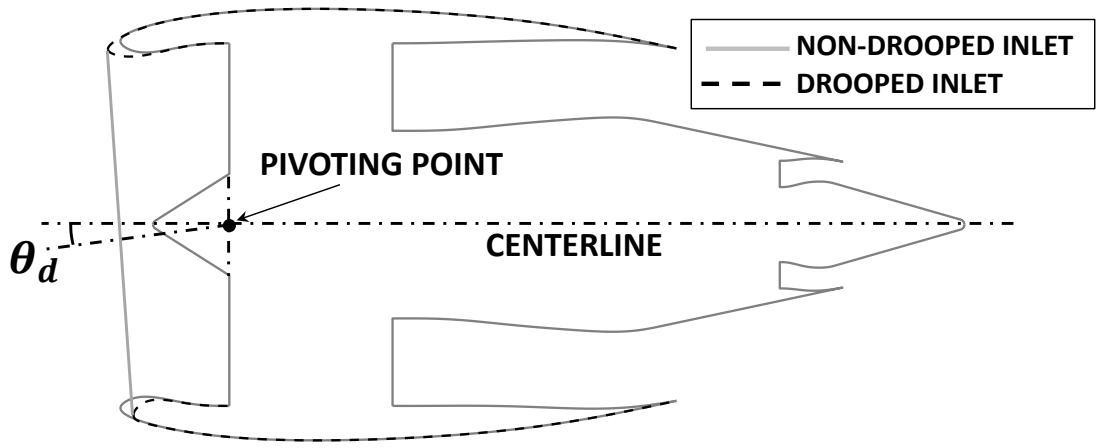

Figure 3.6: Drooped inlet representation.

Particularly for ultra-short nacelles ($L_{inlet}/D_{fan} < 0.4$), the internal lip curvature has shown to have a strong impact on flow separation when the inlet was subjected to either high-incidence or strong crosswinds. Therefore, o allow further control on the lip curvature, a control point was added between the highlight and the throat, for the keel and MHB positions.

3.2 Numerical Approach

After generating the nacelle shape, the commercial software ANSYS ICEM CFD® is used to automatically generate a multiblock fully structured mesh. The computational domain is defined between the nacelle and a cylindrical far-field, with length and diameter equal to 50 times the fan diameter. The height of the wall adjacent cells was

set so that $y^+ < 1$, for the cruise condition, in order to solve the viscous sub-layer. An example of an ultra-short nacelle 3D mesh is shown in Fig. 3.7.

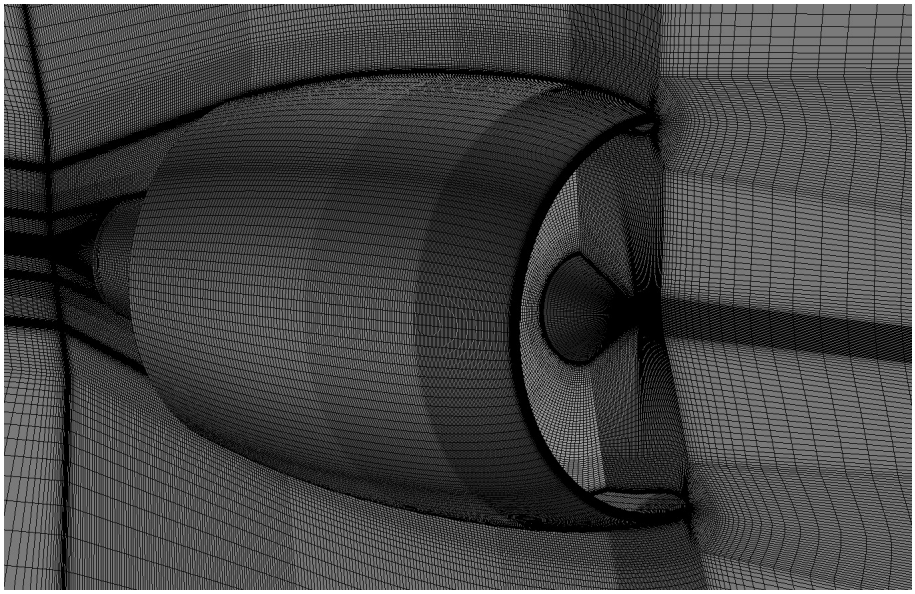

Figure 3.7: Ultra-short nacelle 3D mesh.

The commercially available software ANSYS FLUENT® was used to perform the computational fluid dynamics (CFD) simulations and solve the flow field around the designed nacelle geometries. The computations were performed for the Reynolds-Averaged Navier-Stokes (RANS) equations, using the pressure-based solver, coupled with the $k-\omega$ shear stress transport (SST) turbulence model. The pressure-velocity coupled algorithm was used. The least squares cell based method was used for computation of the flow field gradients and a second order upwind scheme was employed to interpolate the convection terms along with the specific dissipation rate and the turbulent kinetic energy.

To fulfill the entire nacelle design procedure, both 2D axisymmetric and 3D CFD simulations are necessary. However, this work will focus on the 3D computations, since the 2D simulations are merely used as a tool to achieve a preliminary nacelle shape with low computational cost. The 3D simulations start from the obtained 2D axisymmetric design.

Figures 3.8a and 3.8b show a schematic representation for the CFD domain and boundary conditions (BC) employed for the 3D simulations. A pressure outlet BC was set at the fan face, where the static pressure profile and the backflow total temperature were specified. A mass flow target was set to the fan face, allowing the static pressure to vary, in order to assure continuity of mass between the fan and nozzles. Mass flow inlet BCs are specified at the fan and low pressure turbine (LPT) outlets, where mass flow and total temperature are specified. For simulating crosswind operating conditions, the external far-field surface had to be split in 2, as it can be seen in Fig. 3.8b. The windward half was modeled using a pressure-inlet BC, where total pressure and total temperature are specified, whilst the leeward half was set to be a pressure-outlet BC, where static pressure and backflow total

temperature were imposed. For all the remaining cases in the cylindrical outer boundary a pressure-far-field BC was utilized, where freestream static pressure, static temperature, Mach number and flow direction were specified.

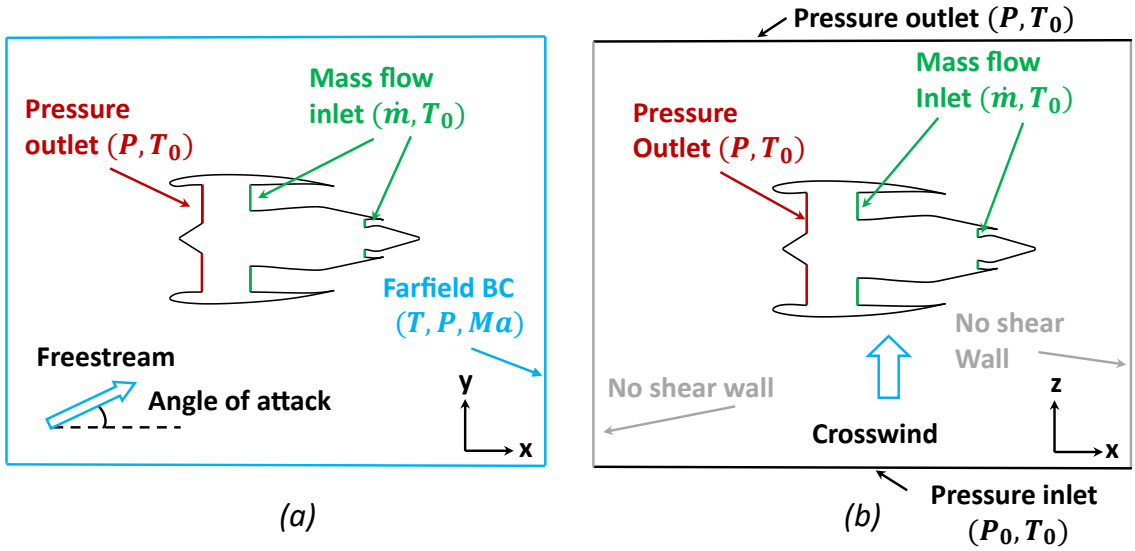

Figure 3.8: Boundary conditions and CFD domain schematic representation.

3.2.1 Fan Face Boundary Condition

.

This section describes a method developed to calculate the pressure profile at the fan face, based on the parallel compressor theory. First, the parallel compressor theory will be briefly described and lastly the developed method will be presented.

The parallel compressor theory consists of a method for modeling the effects of inlet flow distortion, describing the effect of pressure or temperature distortion on both the engine stability and performance [49–51]. In its classical form, the compressor is modeled as two different sectors with different, but uniform, total pressures. The performance of these sectors is represented by mass flow scaled versions of the standard map. Both the compressors discharge to the same static pressure. Therefore, the spoiled compressor, with lower inlet total pressure, will have to operate with a higher pressure ratio, whilst in the clean sector the opposite occurs. Figure 3.9 illustrates the concept, for a spoiled sector of 60 deg.

The aforementioned concept was adapted for CFD applications and used to compute the static pressure profile at the fan face. First, correlations between pressure ratio, efficiency and corrected mass flow are obtained from a typical fan speed line, by linearizing around the engine operating point. The correlations are then used to compute the stagnation pressure and temperature at an imaginary discharge plane, with the same static pressure as the fan exit station. The incoming flow field, computed from the current iteration, is used to do so. Lastly, with knowledge of the pressure ratio and the outlet total pressure, the inlet static and total pressures can be obtained. This procedure is repeated for all the grid points at the fan face.

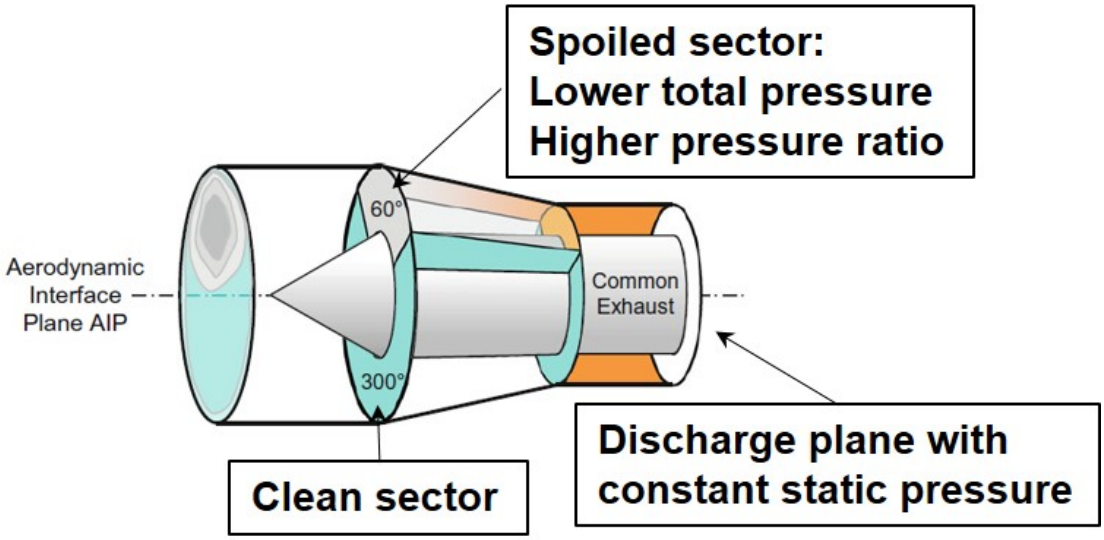

Figure 3.9: Parallel compressor model (Adapted from [51]).

3.3 Aerodynamic Performance Metrics

3.3.1 Thrust and Drag Bookkeeping

A near-field bookkeeping method was used to calculate the net propulsive force, thrust and drag, and assess the nacelle aerodynamic performance at cruise. The boundary surfaces used in the method are depicted in Fig. 3.10. The near-field net propulsive force F_N can be determined from application of the axial momentum balance to a closed surface surrounding nacelle S_{nac} [52–56], as shown in Eq. (3.8).

$$\begin{aligned} F_N &= -\int_{S_{nac}} \left[\rho\left(u-u_\infty\right)\left(\vec{V}\cdot\vec{n}\right)+\left(p-p_\infty\right)n_x-\left(\vec{\tau}_x\cdot\vec{n}\right)\right]dS \\ &= \int_{S_{nac}} \left(\vec{f}\cdot\vec{n}\right)\, dS\,, \end{aligned} \tag{3.8}$$

where $\vec{f}$, following Destarac's [54] notation, is defined as:

$$\vec{f} = \; -\rho\left(u-u_\infty\right)\left(\vec{V}\cdot\vec{n}\right)-\left(p-p_\infty\right)\vec{i}+\left(\vec{\tau}_x\cdot\vec{n}\right)\,. \tag{3.9}$$

The net propulsive force is defined as the difference between thrust and configuration drag, D_c. Therefore, upon choosing one definition for thrust, D_c can be determined. The most commonly utilized definition in bookkeeping systems is the standard net thrust, T_N [52–54, 57].

Classical methods [57, 58] use the inlet entry and nozzles exit surfaces (S_1, S_{18} and S_8) to compute T_N, nevertheless, for CFD applications, it is desired to select locations where the grid is well defined, aiming to avoid interpolation errors. Therefore, the surfaces S_I, S_2, S_S, S_{BN}, S_{CC}, S_{13}, S_{CN}, S_6 and S_P will be used to define T_N. The conservation of momentum applied to the captured and post-exit streamtubes leads

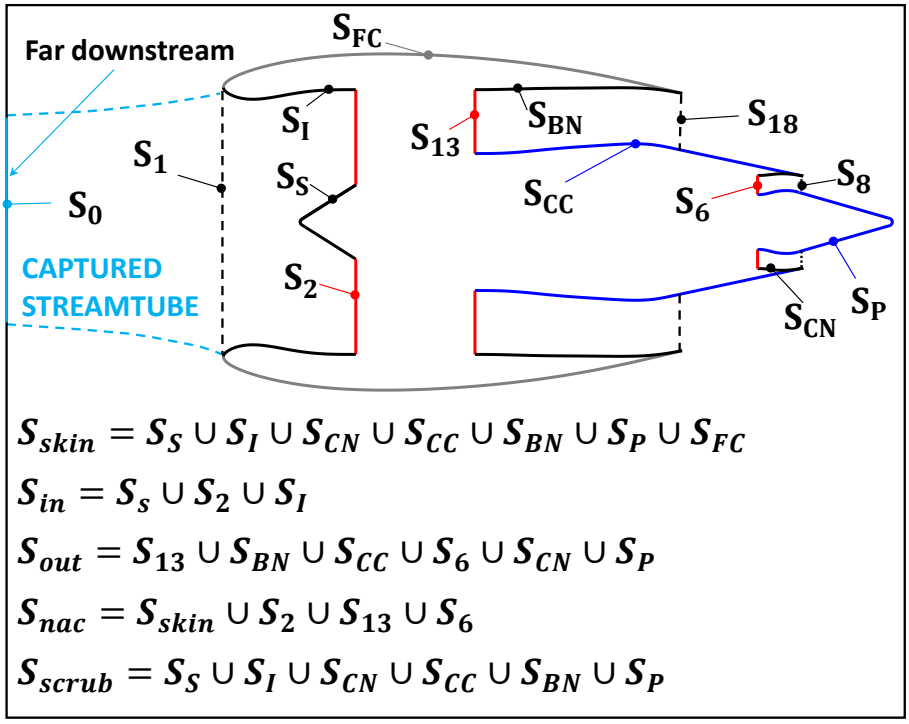

Figure 3.10: Nacelle bookkeeping surfaces.

to the following equation [52, 54]

$$\begin{aligned} T_N = &\int_{S_0} \left[\rho u \left(\vec{V} \cdot \vec{n}\right) + (p - p_\infty)\, n_x - (\vec{\tau}_x \cdot \vec{n})\right] dS \\ &- \int_{S_{out}} \left[\rho u \left(\vec{V} \cdot \vec{n}\right) + (p - p_\infty)\, n_x - (\vec{\tau}_x \cdot \vec{n})\right] dS\,, \end{aligned} \tag{3.10}$$

where S_{out} includes all the surfaces wetted by the exhaust jets. Note that the standard net thrust as presented in Eq. (3.10) is also referred to as "modified standard net thrust" [57], since the forces acting on the external core cowl and plug surfaces are included on it. The configuration drag can then be written as

$$D_c = F_N - T_N\,. \tag{3.11}$$

The fan cowl drag D_{FC} can be defined as

$$D_{FC} = \int_{S_{FC}} \left[(p - p_\infty)\, n_x - (\vec{\tau}_x \cdot \vec{n})\right] dS = (D_p + D_f)_{S_{FC}}\,, \tag{3.12}$$

where D_p is the skin pressure drag, D_f the skin friction drag and S_{FC} is the fan cowl surface.

The pre-entry force F_{pre} is defined as

$$F_{pre} = \int_{S_0 \cup S_{in}} \left[\rho u \left(\vec{V} \cdot \vec{n}\right) + (p - p_\infty)\, n_x - (\vec{\tau}_x \cdot \vec{n})\right] dS\,, \tag{3.13}$$

where S_{in} is comprised of all the inlet surfaces wetted by captured streamtube.

The scrubbing drag D_{scrub} is the skin drag of the internal engine surfaces S_{scrub}, as follows

$$\begin{aligned} D_{scrub} &= \int_{S_{scrub}} \left[(p - p_\infty)\, n_x - (\vec{\tau}_x \cdot \vec{n}) \right] dS \\ &= (D_p + D_f)_{S_{scrub}} \,. \end{aligned} \tag{3.14}$$

Moreover, Eq. (3.8) can be written as follows

$$\begin{aligned} F_N &= \int_{S_{FC} \cup S_{in} \cup S_{out}} \left(\vec{f} \cdot \vec{n} \right) \, dS \\ &= (D_p + D_f)_{S_{FC}} \, + \int_{S_{in} \cup S_{out}} \left(\vec{f} \cdot \vec{n} \right) \, dS \\ &= (D_p + D_f)_{S_{FC}} + F_{pre} - T_N \,, \end{aligned} \tag{3.15}$$

finally, the configuration drag becomes

$$\begin{aligned} D_c &= (D_p + D_f)_{S_{FC}} + F_{pre} \\ &= (D_p + D_f)_{S_{skin}} - (D_p + D_f)_{S_{scrub}} + F_{pre} \,. \end{aligned} \tag{3.16}$$

where S_{skin} is comprised of all skin surfaces wetted by the air passing through and outside of the nacelle. Moreover, the drag coefficient, C_D, can be defined by using the fan face area A_{fan} as reference, as follows

$$c_d = \frac{D_c}{0.5 \rho_\infty V_\infty^2 A_{fan}} \,. \tag{3.17}$$

3.3.2 Inlet and Exhaust Nozzles Performance

For the inlet, the aerodynamic performance was assessed by the means of the mass flow ratio MFR, total pressure distortion coefficient DC_{60} and intake pressure recovery η_i. The MFR, consists of an aerodynamic reference parameter for the inlet and it is defined as the the ratio of the stream-tube captured area, A_0, and the highlight area, A_{hi}, as follows

$$MFR = \frac{A_0}{A_{hi}} \,. \tag{3.18}$$

The DC_{60} coefficient is a standard parameter used to assess the distortion level, which can be defined as

$$DC_{60} = \frac{\overline{P}_{0,fan} - \overline{P}_{0,60}}{\overline{q}} \,, \tag{3.19}$$

where $\overline{P}_{0,fan}$ and $\overline{q}$ are the are averaged total and dynamic pressures at the fan face, and $\overline{P}_{0,60}$ is the area averaged total pressure at the most distorted 60 deg circumferential sector at the fan face. The intake pressure recovery η_i is a measure of how much of the free-stream total pressure is retained after the flow passed through the inlet. It can be defined as follows

$$\eta_i = \frac{\overline{P}_{0,fan}}{P_{0,\infty}}\,, \tag{3.20}$$

where $P_{0,\infty}$ is the free-stream stagnation pressure.

The performance of the bypass and core nozzles can be expressed through the discharge and thrust coefficients, referred to as C_D and C_T respectively. The nozzle performance coefficients are defined as described in [59]. The discharge coefficient of a nozzle can be defined as the ratio of the actual mass flow passing through its throat area to the ideal isentropic mass flow for the same area. The ideal mass flow, $\dot{m}_i$, can be obtained from the isentropic relations for an ideal gas

$$\dot{m}_\mathrm{i} = AP_0 \left(\frac{1}{\lambda}\right)^{\frac{1}{\gamma}} \sqrt{\frac{2\gamma}{(\gamma-1)RT_0}\left(1-\left(\frac{1}{\lambda}\right)^{\frac{\gamma-1}{\gamma}}\right)}\,. \tag{3.21}$$

where the nozzle pressure ratio, λ, is defined as

$$\lambda = \begin{cases} P_0/P_{amb}, & \text{if } P_0/P_{amb} < PR_{crit} \\ PR_{crit}, & \text{if } P_0/P_{amb} \geq PR_{crit}\,. \end{cases} \tag{3.22}$$

and the critical pressure ratio, PR_{crit}, as

$$PR_{crit} = \left(\frac{\gamma+1}{2}\right)^{\frac{\gamma}{\gamma-1}}\,. \tag{3.23}$$

The core and bypass discharge coefficients, can then be respectively written as

$$C_{D_{core}} = \frac{\dot{m}_{core}}{\dot{m}_{i\ core}}\,, \tag{3.24}$$

$$C_{D_{bypass}} = \frac{\dot{m}_{bypass}}{\dot{m}_{i\ bypass}}\,, \tag{3.25}$$

where $\dot{m}_{core}$ and $\dot{m}_{bypass}$ are the actual mass flows in the core and bypass nozzles.

The overall thrust coefficient is defined as the ratio of the actual gross thrust T_{gross} and the sum of the ideal core and bypass nozzle thrusts. The ideal thrust is defined as the product of the actual mass flow and the ideal velocity V_i, resulting from an isentropic expansion to the ambient pressure. The ideal isentropic velocity, V_i, is defined as

$$V_\mathrm{i} = \sqrt{\frac{2\gamma RT_0}{(\gamma-1)}\left(1-\left(\frac{1}{P_0/P_{amb}}\right)^{\frac{\gamma-1}{\gamma}}\right)} \tag{3.26}$$

and hence C_T can be expressed as

$$C_T = \frac{T_{gross}}{\dot{m}_{bypass}V_{i\ bypass} + \dot{m}_{core}V_{i\ core}}\,, \tag{3.27}$$

where the gross thrust produced by the nozzles can be obtained from the integration of momentum flux, static pressure, and shear stress across all the nozzle internal surfaces S_{nozz}.

$$T_{gross} = -\int_{S_{nozz}} \left[\rho u \left(\vec{V} \cdot \vec{n}\right) + (p - p_\infty)\, n_x - (\vec{\tau}_x \cdot \vec{n})\right] dS\,. \tag{3.28}$$

The internal nozzle surfaces, used for the integration of T_{gross} are depicted in Fig. 3.11.

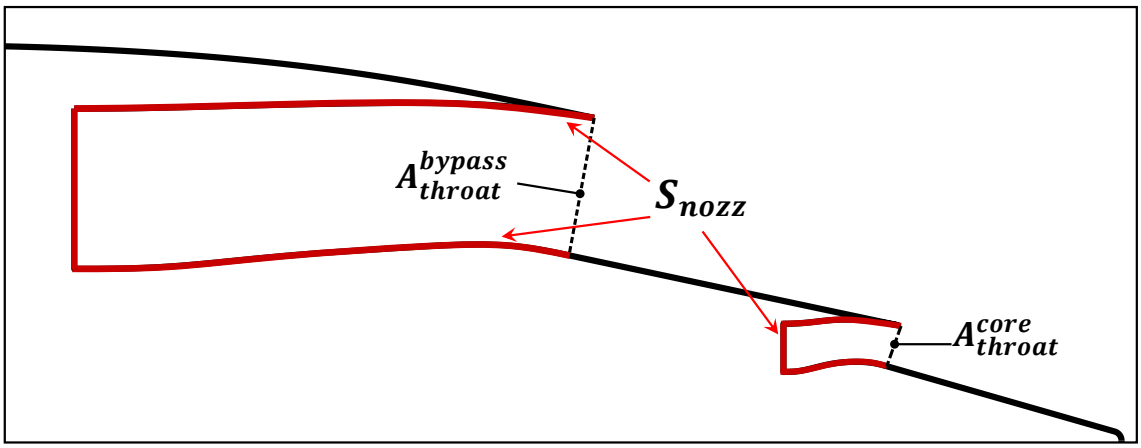

Figure 3.11: Nozzle internal surfaces for computation of T_{gross}.

3.4 Design Procedure

The methods described above were coupled together to form an integrated aerodynamic design framework, comprised of engine cycle calculations, parametric nacelle shape definition, automatic fully structured multi-block mesh generation, 3D RANS CFD computations and aerodynamic performance evaluation. Figure 3.12 presents the flowchart of the overall nacelle design procedure, which can be applied for both conventional length and ultra-short nacelles.

The design procedure starts with the engine design point (DP) cycle calculations for the engine whose nacelle will be designed. After, the operating point of interest is defined and, in case it consists of an off-design operating condition, the off-design point (ODP) cycle calculation is carried out. The commercial software GASTURB® is used to fulfill this first step. Next, the DP output data is used together with the geometry input parameters to shape the nacelle using an in-house MATLAB® code, based on the CST method. Then, the multiblock structured mesh is automatically generated and the 3D RANS CFD computations are performed. The operating point cycle data are used to define the boundary conditions, together with the parallel compressor theory, described in section 3.2.1. The nacelle's aerodynamic performance is then evaluated through thrust and drag bookkeeping, plus the performance metrics described in 3.3.2. In case the established design criteria are not met, new geometric input parameters must be defined and the process should be

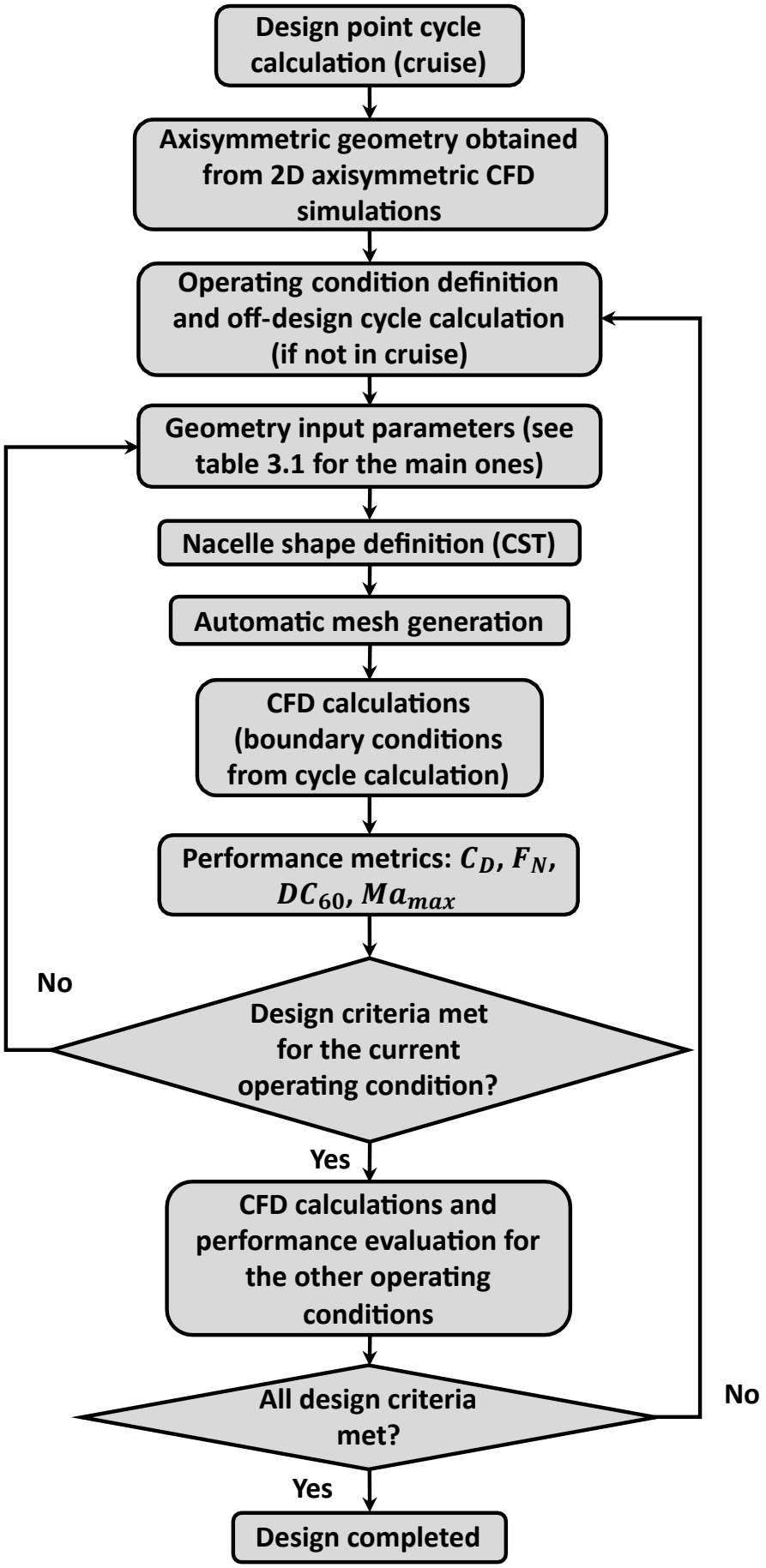

Figure 3.12: Flowchart of the design procedure.

reiterated for the particular operating condition until until the desired performance is achieved. Afterwards, CFD simulations should be performed for all the remaining selected operating conditions. In case the design criteria are not met for some operating condition, new geometric input parameters shall be defined and the process should be reiterated, initially for the current operating point, and lastly for the remaining operating conditions.

This process can be laborious and time demanding, specially due to the high computational time necessary to fulfill all the steps. It is therefore of paramount importance for the designer to have a deep understanding on the flow field behavior and on which parameters play a major role on the nacelle's aerodynamic performance, so that the number of iterations can be minimized.

3.4.1 Operating Conditions

In the early design stage it is not practical to consider all the segments existent in the aircraft mission, due to the high computational costs of 3D CFD simulations. Therefore, only operating conditions considered to be critical were used in this work. The operating conditions shown in Table 3.3, obtained from [17], were used for fulfilling the suggested design approach. The next paragraphs provide a discussion on the motivations behind their choice.

Table 3.3: Operating conditions for the design of nacelles

Condition	Ma	Altitude (m)	AoA (deg)
Cruise	0.8	10668	5
Wing $C_{l_{max}}$	0.25	4267.2	29
Take-off rotation	0.25	0	17
Crosswind	0.0442	0	0

At cruise, the main goal is to minimize drag, therefore shock-waves shall be avoided when possible and the Ma_{max} should be limited. The engine is usually subjected to a local angle of attack AoA approximately equal to 5 deg, caused by the combination of the wing up-wash and the aircraft AoA. Under the wing maximum lift coefficient $C_{L_{max}}$ condition, the aircraft is subjected to the largest angle of attack which is allowed in flight. Although it is not typically encountered in the flight mission, it is important for the certification procedure [17]. In this case, the main concerns are internal inlet separation and distortion levels at the fan entry. The take-off (TO) rotation condition occurs at the end-of-runway, when the aircraft nose is pitching up. Inlet separation and high distortion are also the major problems, since the engine is subjected to relatively high incidence. Aircraft certification requires safe and stable operation at takeoff and landing under a 90-degree cross component of wind velocity. When subjected to crosswind, inlet flow separation can occur, leading to high levels of distortion and possibly to fan surge.

Chapter 4

Experimental Investigation: Nacelle Test Rig

Extensive experimental aerodynamic investigations on nacelles are available in the literature. Flow through nacelles are studied in [60–62], whilst powered nacelles are investigated in [63, 64]. Nonetheless, not enough attention has been given to powered nacelles and, besides, the studies presented are outdated, with nacelle geometries not representative of modern engines and out-of-date measurement techniques. Therefore, there is a need for further aerodynamic investigations of powered-on nacelles with shorter inlets, representative of state-of-the-art and future aero-engines. This chapter presents a powered nacelle test rig designed and built at Chalmers and the first experimental campaign carried out in the Chalmers low-speed wind tunnel. First, the mechanical design of the rig is described and last the preliminary results of the experimental investigation are discussed.

4.1 Rig Description

An axisymmetric nacelle shape was built and mounted around an electric ducted fan (EDF) so that the effects of inlet–fan coupling could be assessed. Figure 4.1 shows the CAD mechanical assembly of the rig. The parts comprising the outer part of the nacelle (lip, midbody upper and lower parts, and afterbody) were assembled together and mounted on the top of two load cells, in order to measure the resultant force. The remaining parts (inlet, nozzle and core cowl) were connected to the EDF, which attached to the strut by means of a fork. This assembly allows the outer nacelle to float in the engine centerline direction, since there is no direct mechanical connection with the fan, and thus the aerodynamic force can be captured by the load cells. Moreover, the split of the inlet and lip was performed in such a way to allow easiness of geometry replacement, so that different geometries cold be tested without need of modifying the rear part of the rig.

The nacelle rig mounted in the wind tunnel is shown in Fig. 4.2. The rig was mounted on the top of a rotary table so that the nacelle could be rotated laterally, allowing variation of angle of attack. The inlet, lip, core cowl and fairing were 3D printed in plastic, whilst the remaining parts were made out of aluminum.

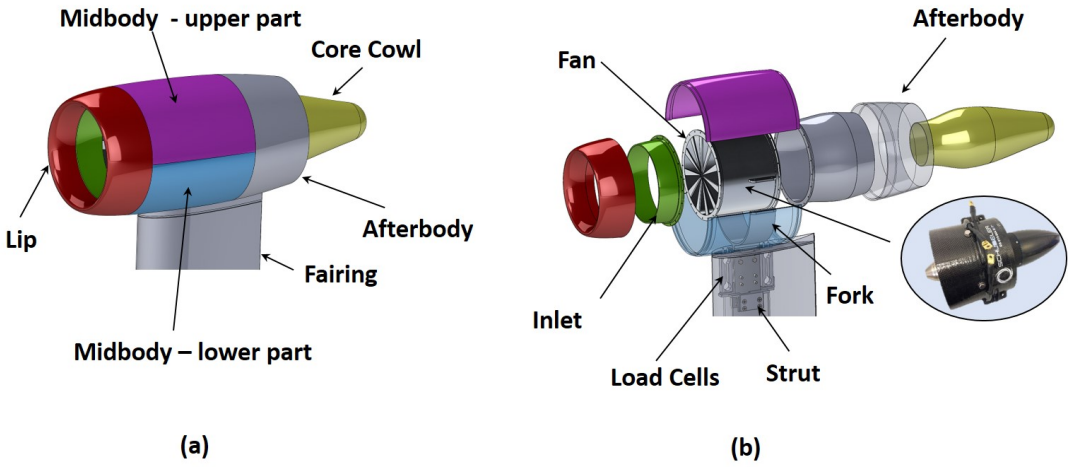

Figure 4.1: Rig assembly.

Figure 4.2: Nacelle rig mounted in the wind tunnel.

4.2 Preliminary Results

The wind tunnel tests were carried out for different AoAs, wind tunnel speeds (WS) and fan rotational speeds. The wind tunnel mapping is shown in Fig. 4.3, where the AoA is varied form 0 to 20 deg and the WS ranges from 10 to 20 m/s. The fan power input request was kept constant, therefore, the rotational speed varied slightly for different cases. The average rotational speed was equal to 7817 rpm. The wind tunnel Reynolds numbers ranged from 2.96×10^5 to 1.48×10^6.

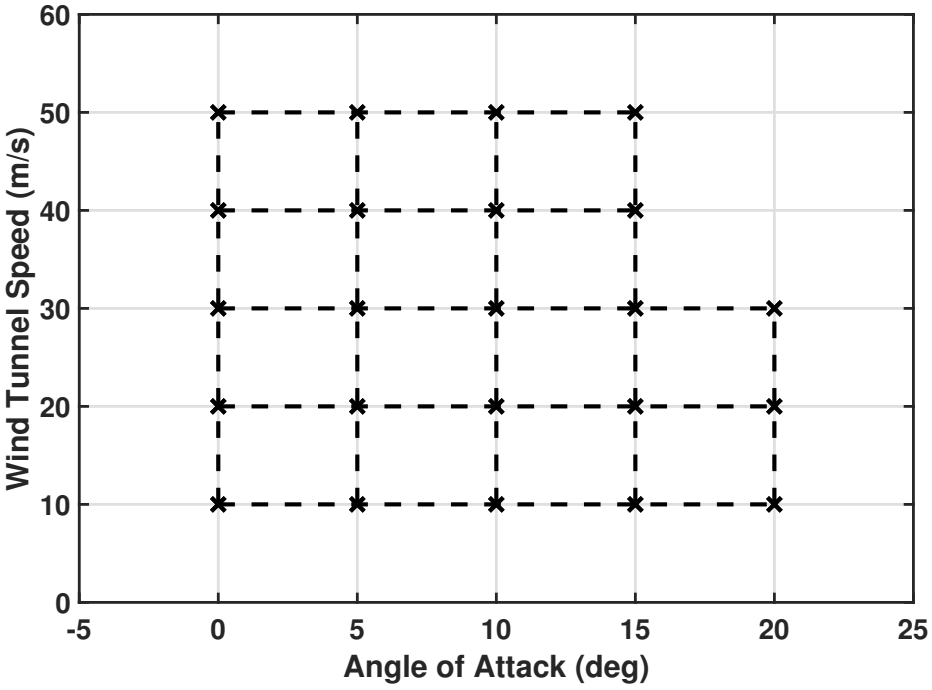

Figure 4.3: Wind tunnel mapping: wind speed versus angle of attack.

The results obtained from the load cells measurements are depicted in Figure 4.4. Note that the force measured here cannot be called drag, because it includes a 'potential flow buoyancy' term, which is the integrated pressure force in potential flow [57]. Moreover, the rig assembly made necessary a 2 mm gap between the lip and the inlet, and thus pressure forces act internally in the outer part of the nacelle. Therefore, a proper drag measurement would require correction for this pressure forces built internally and the implementation of a proper thrust and drag bookkeeping accounting. However, due to the preliminary nature of the first experimental campaign, not enough data is available to do so. It can be observed that the measured force is sometimes negative (points forward) for low WSs. This occurs due to a combination between the mentioned internal pressure forces and the lip suction effect. The latter is caused by an acceleration in the lip throat region, and hence reduction in static pressure. The static pressure acting in the outer part of the nacelle is roughly close to the ambient pressure and thus, the difference between the fan cowl pressure and the internal lip pressure results in a forward force contribution.

The measured force follows similar patterns for the WS varying from 10 to 40 m/s, however, an unusual behavior is observed in the 50 m/s case. This suggests that there might be some internal mechanical interference between the outer nacelle and the fan.

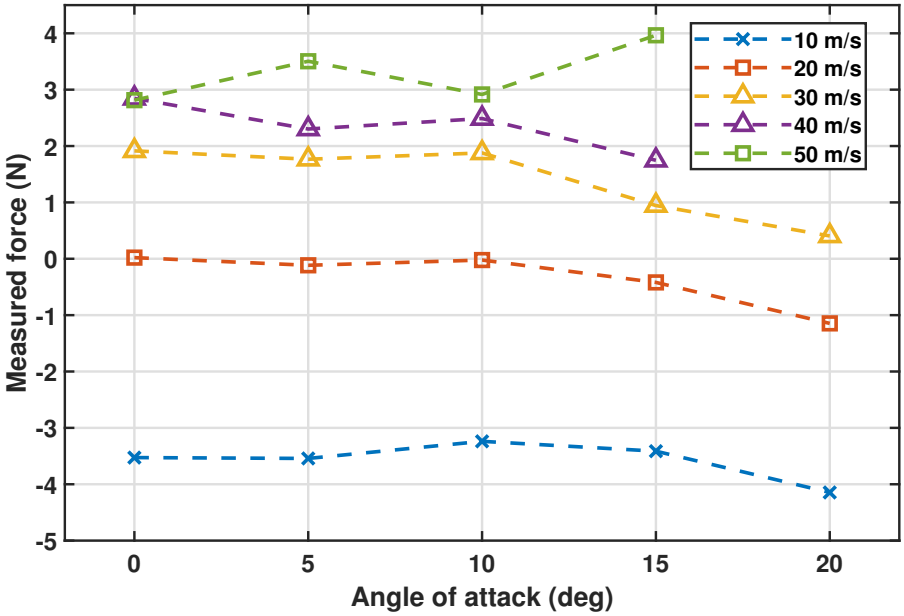

Figure 4.4: Measured force versus angle of attack for different wind tunnel speeds. The power input request was set as 80% of the maximum power.

A second set of measurements were obtained by keeping the AoA and wind tunnel speeds constant and by varying the fan power input request, and thus the rotational speed. The MFR versus the outer nacelle force is plotted in Fig. 4.5 for AoA=0 deg, WS=10 m/s and power input requests ranging from 40 to 100% of the maximum power. The MFR could be estimated placing a pressure tap just upstream of the fan face, on the inlet surface. By assuming a inlet total pressure loss, the average Mach number on the fan face could be calculated and, therefore, the mass flow and the captured stream-tube area. It can be observed that the measured force increases with the MFR, and this is likely to be caused by an increased pre-entry force F_{pre}, due to an higher captured stream-tube momentum flux.

To assess the influence of the fan on the nacelle flow-field, surface tufts were placed on the leeward side of the fan cowl and on the windward side of the internal lip, where separation is more likely to occur. Figure 4.6 shows the flow visualization results for AoA=10 deg, WS=30 m/s. On the top pictures, the fan was off, whilst in the bottom ones the fan rotational speed was equal to 7750 RPM. A separation bubble could be observed when the fan was off, however when the fan was turned on, the boundary layer was re-energized and the flow reattached. This, as expected, is an indication that the fan can strongly influence the nacelle internal and external flow, and it justifies the construction of a powered nacelle rig instead of a simpler flow-through nacelle one.

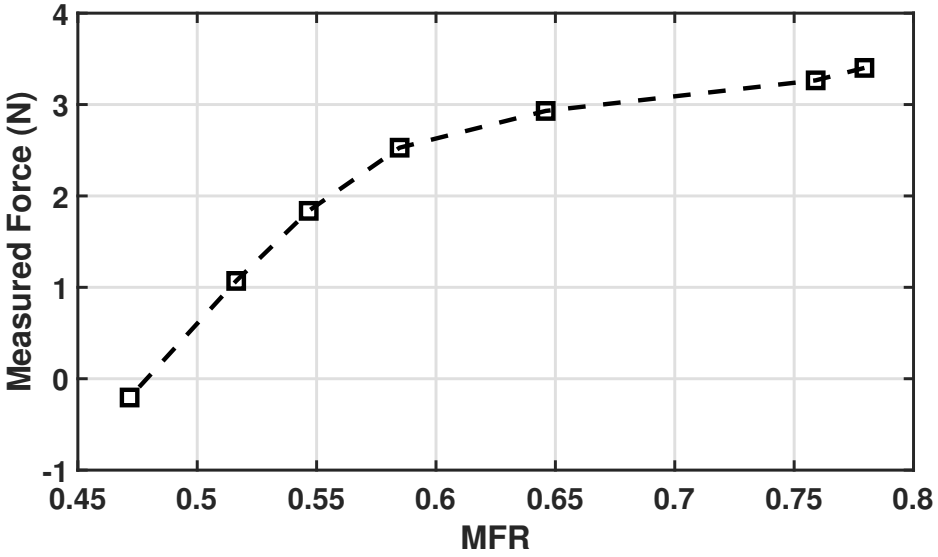

Figure 4.5: Variation of the measured force with mass flow ratio for AoA=0 deg, WS=10 m/s.

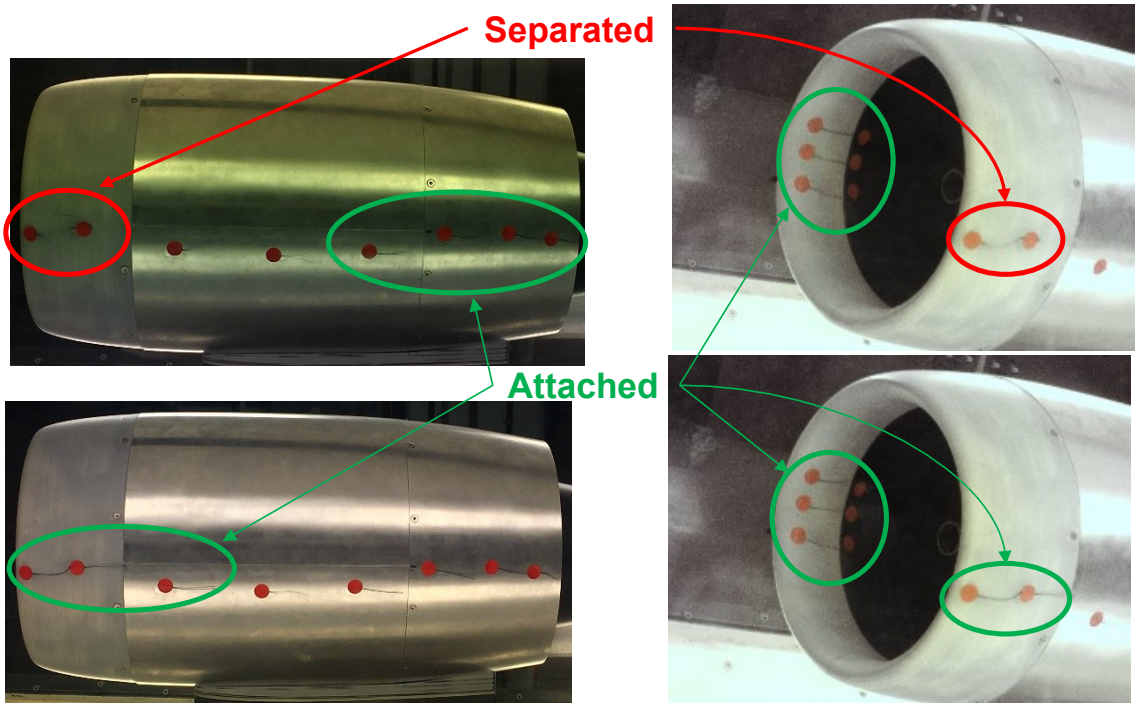

Figure 4.6: Flow visualization for AoA=10 deg and wind speed=30 m/s. The top figures show the results obtained when the fan was off. On the bottom figures, the fan rotational speed was equal to 7750 RPM. The surface tufts were attached to the leeward part of the fan cowling and to the windward part of the internal lip.

Chapter 5

Summary of Papers

5.1 Paper A

V. T. Silva, A. Lundbladh, C. Xisto, O. Petit, 2020, "Multi-point aerodynamic design of ultra-short nacelles for ultra-high bypass turbofan engines". *To be submitted to a scientific journal*

5.1.1 Division of work

I, as the main author, developed the integrated design framework used to construct the nacelle geometries presented in this paper. Moreover all the methods here presented were implemented by myself and all the meshing and the CFD simulations were done by me. Anders Lundbladh have contributed with key ideas for the development of this work, such as boundary conditions, thrust and drag bookkeeping and geometry generation methods. Among his suggestions, the idea to use the parallel compressor theory to derive the static pressure profile at the fan face stands out. Carlos Xisto and Olivier Petit supervised the work and provided useful feedback to improve the article.

5.1.2 Summary and Discussion

This paper presents a new methodology for multi-point aerodynamic design of ultra-short nacelles for ultra-high-bypass turbofan engines. The major design parameters are identified and their influence in the flowfield is discussed in detail for the selected operating conditions. The developed tools have proven to be suitable for designing ultra-short nacelles capable of performing well under the most critical flight conditions, such as high angle of attach, cruise and crosswind. Crosswind was found to be the most impacting condition in the design procedure, requiring a severe shape modification to meet the design criteria. Furthermore, a significant increase in drag was the result of designing a separation-free inlet at the crosswind condition.

Chapter 6

Concluding Remarks

The main goal of this thesis was to provide a step further on the design of ultra-short nacelles for ultra-high bypass turbofan engines. A novel methodology for performing multi-point design of ultra-short nacelles was presented and several test cases were defined to assess the impact of the major design parameters in the flow field. The developed tools have proven to be suitable for designing ultra-short nacelles capable of performing well under the most critical operating conditions, which were cruise, crosswind and high angle-of-attack. Crosswind has shown to be the most impacting condition in the design procedure, requiring a severe shape modification to meet the design criteria. Furthermore, a significant increase in drag was the result of designing a separation-free inlet at the crosswind condition.

A secondary goal was to present the results of an experimental aerodynamic investigation on a powered nacelle carried out at the Chalmers low speed wind tunnel. The test rig assembly was described in summary and the preliminary results from the first test campaign were discussed. The experimental research works as a first step towards more advanced configurations and measurement techniques.

6.1 Future Work

Future work should focus on evaluating more integrated geometries, including pylons, wings and fuselage, thus allowing to assess how the interference effects impact the design of ultra-short nacelles. Moreover, innovative configurations shall also be studied, possibly employing boundary layer ingestion and engines more closely coupled to the fuselage.

Bibliography

[1] Darecki, M and Edelstenne, C and Enders, T and Fernandez, Emma and Hartman, Peter and Herteman, Jean-Paul and Kerkloh, Michael and King, Ian and Ky, Patrick and Mathieu, Michel and others. "Flightpath 2050 Europe's vision for aviation". In: *Off. Eur* (2011).

[2] Dale E Van Zante. "Advances in Turbofan Engines: A US Perspective". In: *Encyclopedia of Aerospace Engineering* (2010), pp. 1–12.

[3] W Bauermeister and H IP. "727 airplane engine inlet development". In: *4th Propulsion Joint Specialist Conference*. 1968, p. 595.

[4] JE McCall, P Tracksdorf, and K Heinig. "Advanced ducted engine nacelle aerodynamics and integration testing". In: (1992).

[5] H Hoheisel. "Aerodynamic aspects of engine-aircraft integration of transport aircraft". In: *Aerospace science and technology* 1.7 (1997), pp. 475–487.

[6] WS Viall. *Aerodynamic Considerations for Engine Inlet Design for Subsonic High Bypass Fan Engines*. Tech. rep. SAE Technical Paper, 1966.

[7] WM Douglass. *Aerodynamic Installation of High-Bypass-Ratio Fan Engines*. Tech. rep. SAE Technical Paper, 1966.

[8] H Kuenkler et al. "An investigation of very high bypass ratio engines for subsonic transports". In: *Journal of Propulsion and Power* 6.4 (1990).

[9] TJ Barber et al. "Computational design and validation tests of advanced concept subsonic inlets". In: *Journal of Propulsion and Power* 1.2 (1985), pp. 97–102.

[10] HC Potonides. "Development of an inlet for a tilt nacelle subsonic V/STOL aircraft". In: (1979).

[11] M Sussman, D Gunnarson, and P Edwards. "Nacelle design studies for advanced transport aircraft". In: *8th Joint Propulsion Specialist Conference*. 1972, p. 1204.

[12] M Mackinnon and B Metha. "Factors influencing nacelle design on the 747". In: *15th Joint Propulsion Conference*. 1979, p. 1236.

[13] J Malone, J Vadyak, and L Sankar. "A technique for the inverse aerodynamic design of nacelles and wing configurations". In: *3rd Applied Aerodynamics Conference*. 1985, p. 4096.

[14] RA Bell and RD Cedar. "An inverse method for the aerodynamic design of three-dimensional aircraft engine nacelles". In: (1991).

[15] Roland Wilhelm. “An inverse design method for engine nacelles and wings”. In: *Aerospace science and technology* 9.1 (2005), pp. 19–29.

[16] Roland Wilhelm. “Inverse design method for designing isolated and wing-mounted engine nacelles”. In: *Journal of aircraft* 39.6 (2002), pp. 989–995.

[17] Andreas Peters et al. “Ultrashort Nacelles for Low Fan Pressure Ratio Propulsors”. In: *Journal of Turbomachinery* 137.2 (Sept. 2014). 021001. ISSN: 0889-504X. DOI: 10.1115/1.4028235.

[18] R Schnell and J Corroyer. “Coupled fan and intake design optimization for installed UHBR-engines with ultra-short nacelles”. In: *23rd International Symposium on Air Breathing Engines ISABE*. 2015.

[19] Nagabhushana Rao Vadlamani et al. “Toward Future Installations: Mutual Interactions of Short Intakes With Modern High Bypass Fans”. In: *Journal of Turbomachinery* 141.8 (July 2019). ISSN: 0889-504X. DOI: 10.1115/1.4044080.

[20] H Riedel et al. “Aerodynamic design of a natural laminar flow nacelle and the design validation by flight testing”. In: *Aerospace science and technology* 2.1 (1998), pp. 1–12.

[21] AJ Mullender and DIA Poll. “Natural and Hybrid Laminar Flow Control for Aero-Engine Nacelles”. In: *SAE transactions* (1995), pp. 1477–1487.

[22] H Riedel, A Ronzheimer, and M Sitzmann. “Analysis of the static pressure distribution on a laminar flow nacelle based on euler calculations and flight measurements”. In: *Aerospace science and technology* 2.2 (1998), pp. 129–143.

[23] R Radespiel, KH Horstmann, and G Redeker. “Feasibility study on the design of a laminar flow nacelle”. In: *Journal of Aircraft* 27.11 (1990), pp. 959–965.

[24] Vermeersch and Xavier Bouteiller. “Numerical study of laminar nacelles: natural and hybrid laminar flow designs”. In: *International Journal of Engineering Systems Modelling and Simulation 48* 6.3-4 (2014), pp. 191–204.

[25] Tomasz P Stańkowski and David G MacManus and Christopher TJ Sheaf and Robert Christie. “Aerodynamics of aero-engine installation”. In: *Proceedings of the Institution of Mechanical Engineers, Part G: Journal of Aerospace Engineering* 230.14 (2016), pp. 2673–2692. DOI: 10.1177/0954410016630332.

[26] Robert Christie et al. “The use of hybrid intuitive class shape transformation curves in aerodynamic design”. In: *Aerospace Science and Technology* 95 (2019), p. 105473.

[27] Anders Lundbladh et al. “Installation effects for ultra-high bypass engines”. In: *Proceedings of the 23rd International Symposium on Air Breathing Engines, ISABE-2017*. 2017.

[28] Fernando Tejero et al. “Multi-objective optimisation of short nacelles for high bypass ratio engines”. In: *Aerospace Science and Technology* 91 (2019), pp. 410–421. ISSN: 1270-9638. DOI: https://doi.org/10.1016/j.ast.2019.02.014.

[29] Fernando Tejero, David G. MacManus, and Christopher Sheaf. "Surrogate-based aerodynamic optimisation of compact nacelle aero-engines". In: *Aerospace Science and Technology* 93 (2019), p. 105207. ISSN: 1270-9638.

[30] Fernando Tejero, David MacManus, and Christopher Sheaf. "Impact of Droop and Scarf on the Aerodynamic Performance of Compact Aero-Engine Nacelles". In: *AIAA Scitech 2020 Forum*. 2020, p. 1522.

[31] Ioannis Goulos et al. "Aerodynamic Design of Separate-Jet Exhausts for Future Civil Aero-engines—Part I: Parametric Geometry Definition and Computational Fluid Dynamics Approach". In: *Journal of Engineering for Gas Turbines and Power* 138.8 (Mar. 2016). 081201. ISSN: 0742-4795. DOI: 10.1115/1.4032649.

[32] Ioannis Goulos et al. "Aerodynamic Design of Separate-Jet Exhausts for Future Civil Aero-engines—Part II: Design Space Exploration, Surrogate Modeling, and Optimization". In: *Journal of Engineering for Gas Turbines and Power* 138.8 (Mar. 2016). 081202. ISSN: 0742-4795. DOI: 10.1115/1.4032652.

[33] John J. Otter et al. "Parametric design of non-axisymmetric separate-jet aero-engine exhaust systems". In: *Aerospace Science and Technology* 93 (2019), p. 105186. ISSN: 1270-9638. DOI: https://doi.org/10.1016/j.ast.2019.05.038.

[34] Luís Gustavo Trapp and Roberto da Motta Girardi. "Crosswind Effects on Engline Inlets: The Inlet Vortex". In: *Journal of aircraft* 47.2 (2010), pp. 577–590.

[35] Kiran Vunnam and Robert Hoover. "Modeling of Inlet Distortion Using a Combined Turbofan and Nacelle Inlet Model During Crosswind and Low Speed Forward Operation". In: vol. Volume 1: Aircraft Engine; Ceramics; Coal, Biomass and Alternative Fuels; Wind Turbine Technology. Turbo Expo: Power for Land, Sea, and Air. June 2011, pp. 371–380.

[36] Yeung, Alex and Vadlamani, Nagabhushana Rao and Hynes, Tom and Sarvankar, Sumit. "Quasi 3D Nacelle Design to Simulate Crosswind Flows: Merits and Challenges". In: *International Journal of Turbomachinery, Propulsion and Power* 4.3 (2019), p. 25.

[37] Kuen-Bae Lee, Mark Wilson, and Mehdi Vahdati. "Effects of Inlet Disturbances on Fan Stability". In: *Journal of Engineering for Gas Turbines and Power* 141.5 (Dec. 2018). 051014. ISSN: 0742-4795. DOI: 10.1115/1.4042204.

[38] Ed Obert. *Aerodynamic design of transport aircraft*. IOS press, 2009.

[39] John Seddon and E Laurie Goldsmith. *Intake aerodynamics*. Vol. 2. Blackwell science Boston, 1999.

[40] Jeff Borland et al. *Drag of axisymmetric cowls at zero incidence for subsonic Mach numbers*. ESDU, 1994.

[41] Brenda M Kulfan. "Universal parametric geometry representation method". In: *Journal of aircraft* 45.1 (2008), pp. 142–158.

[42] Feng Zhu and Ning Qin. "Intuitive class/shape function parameterization for airfoils". In: *AIAA journal* 52.1 (2014), pp. 17–25.

[43] Robert Christie, Alexander Heidebrecht, and David MacManus. "An Automated Approach to Nacelle Parameterization Using Intuitive Class Shape Transformation Curves". In: *Journal of Engineering for Gas Turbines and Power* 139.6 (Jan. 2017). 062601. ISSN: 0742-4795. DOI: 10.1115/1.4035283.

[44] Tomasz P. Stankowski et al. "Aerodynamic Effects of Propulsion Integration for High Bypass Ratio Engines". In: *Journal of Aircraft* 54.6 (May 2017), pp. 1–15.

[45] Matthew Robinson and David G MacManus and Christopher Sheaf. "Aspects of aero-engine nacelle drag". In: *Proceedings of the Institution of Mechanical Engineers, Part G: Journal of Aerospace Engineering* 233.5 (2019), pp. 1667–1682. DOI: 10.1177/0954410018765574.

[46] Dennis L Berry. "The Boeing 777 Engine/Airframe Integration Aerodynamic Design Process". In: *ICAS PROCEEDINGS*. Vol. 19. AMERICAN INST OF AERONAUTICS and ASTRONAUTICS. 1994, pp. 1305–1305.

[47] Norbert O Stockman, David E Yates, and Timothy S Crum. *Nacelle inlet for an aircraft gas turbine engine*. US Patent 5,058,617. Oct. 1991.

[48] William C Ruehr, James L Younghans, and Edwin B Smith. *Curved centerline air intake for a gas turbine engine*. US Patent 4,220,171. July 1980.

[49] William T. Cousins and Jr. Davis Milt W. "Evaluating Complex Inlet Distortion With a Parallel Compressor Model: Part 1—Concepts, Theory, Extensions, and Limitations". In: vol. Volume 1: Aircraft Engine; Ceramics; Coal, Biomass and Alternative Fuels; Wind Turbine Technology. Turbo Expo: Power for Land, Sea, and Air. June 2011, pp. 1–12.

[50] Jr. Davis Milt W. and William T. Cousins. "Evaluating Complex Inlet Distortion With a Parallel Compressor Model: Part 2—Applications to Complex Patterns". In: vol. Volume 1: Aircraft Engine; Ceramics; Coal, Biomass and Alternative Fuels; Wind Turbine Technology. Turbo Expo: Power for Land, Sea, and Air. June 2011, pp. 13–23. DOI: 10.1115/GT2011-45068.

[51] Joachim Kurzke and Ian Halliwell. *Propulsion and Power: An Exploration of Gas Turbine Performance Modeling*. Springer, 2018.

[52] Benoit Malouin et al. "Engine pre-entry thrust and standard net thrust evaluation based on the far-field method". In: *Aerospace Science and Technology* 45 (2015), pp. 50–59. ISSN: 1270-9638. DOI: https://doi.org/10.1016/j.ast.2015.04.014.

[53] Benoit Malouin, Jean-Yves Trepanier, and Eric Laurendeau. "Installation and interference drag decomposition via RANS far-field methods". In: *Aerospace Science and Technology* 54 (2016), pp. 132–142. ISSN: 1270-9638. DOI: https://doi.org/10.1016/j.ast.2016.04.020.

[54] D. Destarac and J. Van der Vooren. "Drag/thrust analysis of jet-propelled transonic transport aircraft; Definition of physical drag components". In: *Aerospace Science and Technology* 8.6 (2004), pp. 545–556. ISSN: 1270-9638. DOI: https://doi.org/10.1016/j.ast.2004.03.004.

[55] Renato Tognaccini. "Drag computation and breakdown in power-on conditions". In: *Journal of aircraft* 42.1 (2005), pp. 245–252.

[56] C. P. van Dam. "Recent experience with different methods of drag prediction". In: *Progress in Aerospace Sciences* 35.8 (Nov. 1999), pp. 751–798. DOI: 10.1016/S0376-0421(99)00009-3.

[57] Ministry-Industry Drag Analysis Panel Study Group and others. *Guide to In-Flight Thrust Measurement of Turbojets and Fan Engines*. Tech. rep. AGARD-AG-273, Jan, 1979.

[58] Eugene C Rooney. "Thrust-Drag Accounting Methodology". In: *Thrust and Drag: Its Prediction and Verification* 98 (1985), pp. 31–95.

[59] Kevin L Mikkelsen et al. "Initial subscale performance measurements of the AIAA dual separate flow reference (DSFR) nozzle". In: *51st AIAA/SAE/ASEE Joint Propulsion Conference*. 2015, p. 3883.

[60] Melissa Rivers and Ashley Dittberner. "Experimental investigations of the nasa common research model in the nasa langley national transonic facility and nasa ames 11-ft transonic wind tunnel". In: *49th AIAA aerospace sciences meeting including the new horizons forum and aerospace exposition*. 2011, p. 1126.

[61] MS Zawislak, DJ Cerantola, and AM Birk. "Identifying opportunities for reducing nacelle drag". In: *Journal of Engineering for Gas Turbines and Power* 140.2 (2018).

[62] Michael J Larkin and Paul S Schweiger. "Ultra high bypass nacelle aerodynamics inlet flow-through high angle of attack distortion test". In: (1992).

[63] Kazuhiro Kusunose, James Crowder, and Gregory Miller. "Installed powered engine effects on drag using a wake-integral method". In: *Fluids 2000 Conference and Exhibit*. 2000, p. 2400.

[64] GW Brune. "Quantitative three-dimensional low-speed wake surveys". In: (1992).